

Algorithms for magnetic tomography - on the role of a priori knowledge and constraints

Karl-Heinz Hauer¹, Roland Potthast² and Martin Wannert³

¹TomoScience GbR, Major-Hirst-Str. 11 (Innovationscampus), 38442 Wolfsburg, Germany

²Department of Mathematics, University of Reading, Whiteknights, PO Box 220, Berkshire, RG6 6AX, UK

³Forschungszentrum Jülich, Institute of Energy Research - Fuel Cells (IEF-3), 52425 Jülich, Germany

E-mail: kh.hauer@xcellvision.com, r.w.e.potthast@reading.ac.uk and m.wannert@fz-juelich.de

Abstract. Magnetic tomography investigates the reconstruction of currents from their magnetic fields. Here, we will study a number of *projection methods* in combination with the Tikhonov regularization for stabilization for the solution of the Biot-Savart integral equation $Wj = H$ with the Biot-Savart integral operator $W : (L^2(\Omega))^3 \rightarrow (L^2(\partial G))^3$ where $\bar{\Omega} \subset G$. In particular, we study the role of a priori knowledge when incorporated into the choice of the projection spaces $X_n \subset (L^2(\Omega))^3$, $n \in \mathbb{N}$, for example the conditions $\operatorname{div} j = 0$ or the use of the full boundary value problem $\operatorname{div} \sigma \operatorname{grad} \varphi_E = 0$ in Ω , $\nu \cdot \sigma \operatorname{grad} \varphi_E = g$ on $\partial\Omega$ with some known function g , where $j = \sigma \operatorname{grad} \varphi_E$ and σ is an anisotropic matrix valued conductivity.

We will discuss and compare these schemes investigating the ill-posedness of each algorithm in terms of the behaviour of the singular values of the corresponding operators both when a priori knowledge is incorporated and when the geometrical setting is modified. Finally, we will numerically evaluate the stability constants in the practical setup of magnetic tomography for fuel cells and, thus, calculate usable error bounds for this important application area.

Submitted to: *Inverse Problems*

1. Introduction

Magnetic tomography is concerned with the reconstruction of currents from their magnetic fields. Current reconstructions are of importance for several practical applications. In medicine the magnetic fields around the brain reflect the neural activity in different areas of the animal or human being. The location of source distributions is important for planning of surgery and as a general means of diagnosis. Industrial applications use magnetic fields in such diverse areas as steel production and fuel cells. For the fuel cell application the reconstruction of current densities is needed for the

development, monitoring and testing of the chemical and physical processes in fuel cells.

Here, our goal is to a) formulate algorithms for current reconstruction which incorporate different conditions arising from a priori knowledge about the unknown current density and b) to investigate the ill-posedness of different algorithms for magnetic tomography in the setting which is employed in the fuel cell application area. First, we describe the background and geometrical setup of the reconstruction problem.

Fuel cells are chemical devices which transform chemical energy into electrical energy. The basic principle for a hydrogen-oxygen fuel cell is shown in Figure 1. At the anode (-) hydrogen is inserted. Air or oxygen, respectively, is fueled at the cathode (+). They are separated by a semi-permeable membrane for protons coated with some catalysor (for example platinum). Protons move to the cathode through the membrane. This creates a potential which then drives electrons through an external wire and power some motor or light. Hydrogen and oxygen react at the cathode to water and heat. Usually fuel cells need some heating and cooling technology.

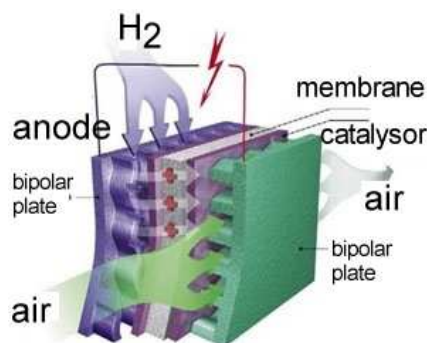


Figure 1. We show the principle of a fuel cell. Hydrogen and oxygen are fueled into different layers. They react, creating a potential which drives electric currents through the wires.

Magnetic tomography in biomedical applications has a long history. We refer the reader to the survey articles [4], [16] and [2] with extensive literature. Basic mathematical results can be found in the books of Kaipio-Somersalo [8] and Kirsch [9]. To our knowledge, the study of the ill-posedness of the magnetic tomography problem with respect to the use of a priori knowledge has not yet been carried out.

In contrast to the medical applications, the currents in fuel cells do *not have internal sources*. This leads to an underlying partial differential equations without source terms on the right-hand side. It strongly influences the uniqueness results (usually in the medical setting the location and polarization of sources is reconstructed) and to some extent the reconstruction techniques (in medical applications often a finite number of parameters is determined searching for source locations).

The basic setting of *magnetic tomography for fuel cells* has been investigated in a series of papers on *numerical simulations* with the Tikhonov regularization for reconstruction [12], on the underlying *anisotropic forward problem* via the finite

integration technique [13], on the *uniqueness question* for current reconstructions in single cell devices [7] and in full stacks [5] and on the full applied *measurement method* including the design of a machine for such measurements [6]. In [14] the resolution of the reconstructed current density depending on the relative error in the magnetic field measurements is discussed. Sampling and probe methods for magnetic tomography have been investigated in [11] and [15]. More general introductions into solution techniques for inverse problems can be found in [3] and [1].

Next, we describe the underlying model from which parts will be incorporated into our reconstruction algorithms later. Consider a geometrical setting as shown in Figure 2. We will model the active area of the fuel cell as a simple cube, where current is injected into the cube at some point on the bottom and is flowing out at another point on the back side. This means we know the total current in the cell and, in particular, we know the inflowing and outflowing current on the boundary of the domain Ω . This leads to the boundary condition

$$\nu \cdot j(y) = g, \quad y \in \partial\Omega \quad (1)$$

with some given function g on $\partial\Omega$. In this work we will restrict our attention to the static situation, where the currents j do not depend on time. The behaviour of time-independent currents, electric and magnetic fields is governed by the stationary *Maxwell equations*

$$\nabla \times H = j, \quad \nabla \times E = 0 \quad (2)$$

$$\nabla \cdot D = \rho, \quad \nabla \cdot B = 0 \quad (3)$$

complemented by the *material equations*

$$D = \epsilon\epsilon_0 E, \quad B = \mu\mu_0 H \quad (4)$$

and *Ohm's law*

$$j = \sigma E. \quad (5)$$

Here, E is the electric field, D the electric flux density, H the magnetic field strength, B the magnetic flux density, j the current density, ρ the electric charge density, σ the conductivity distribution, ϵ the electric permittivity and μ the magnetic permeability of the medium under consideration, ϵ_0 and μ_0 are the well-known natural constants for the vacuum. For the fuel-cell application equations (5) - (6) are a macroscopic model with some *effective* conductivity σ with summarizes the influence of chemical processes, fluid dynamics of oxygen and hydrogen and the shape of the flow field into some mesoscopic variable.

The above equations are usually transformed into an elliptic boundary value problem, [13], for which then unique solvability is shown. Assume that Ω is simply connected. Because of $\nabla \times E = 0$ there is an *electric potential* φ_E such that $E = \nabla\varphi_E$, i.e. for the current density j we have the equation $j = \sigma\nabla\varphi_E$. We use the identity

$\nabla \cdot \nabla \times A = 0$, which is valid for any arbitrary sufficiently smooth vectorfield A , to derive the equation

$$\nabla \cdot j = \nabla \cdot \nabla \times H = 0 \quad (6)$$

from the Maxwell equations (2), i.e. the current distribution is *divergence free*. This will be one of the conditions included into the inversion later. Now, we obtain the equation

$$\nabla \cdot \sigma \nabla \varphi_E = 0 \quad \text{in } \Omega \quad (7)$$

for the electric potential φ_E . Additionally, we have the boundary condition

$$\nu \cdot j = \nu \cdot \sigma \nabla \varphi_E = g \quad (8)$$

mentioned above. We further require the additional *normalization condition*

$$\int_{\Omega} \varphi_E dy = 0 \quad (9)$$

to establish uniqueness for this particular *Neumann problem*, compare [13].

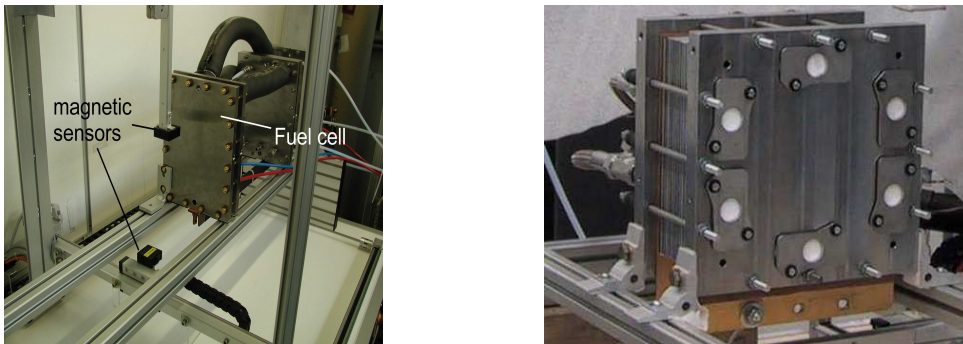


Figure 2. We show a fuel cell (left) and fuel cell stack (right) in the laboratory. The magnetic tomograph is seen in the left image with two magnetic sensors. By courtesy of TomoScience GbR, Wolfsburg / Research Center Jülich, Germany

Let us now assume that we know the current distribution j in the domain $\Omega \subset \mathbb{R}^3$. Magnetic fields H of currents j are calculated via the *Biot-Savart integral operator*, defined by

$$(Wj)(x) := \frac{1}{4\pi} \int_{\Omega} \frac{j(y) \times (x - y)}{|x - y|^3} dy, \quad x \in \mathbb{R}^3 \quad (10)$$

for a current density distribution $j \in L^2(\Omega)^3$. The task of magnetic tomography in its general form reduces to solving the equation

$$Wj = H_{\text{meas}} \quad \text{on } \partial G, \quad (11)$$

where G is some domain with sufficiently smooth boundary such that $\bar{\Omega} \subset G$ and H_{meas} denotes some measured magnetic field on ∂G . As discussed in [12], in principle it is sufficient to know the normal component of H on the measurement surface ∂G . However, we will work with the full field H , i.e. with redundant data which is used in

the practical applications (compare Figure 2) to obtain a better control of measurement error.

The *nullspace* of the Biot-Savart integral operator was studied in detail in [5], where a characterization of $N(W)$ and its orthogonal space $N(W)^\perp$ has been derived. In particular, we have

$$N(W) = \{\text{curl } v : v \in H_0^1(\Omega)^3, \text{div } v = 0\} \quad (12)$$

with $H_0^1(\Omega) := \{v \in H^1(\Omega)^3 : v|_{\partial\Omega} = 0\}$. Additionally, the orthogonal complement of $N(W)$ with respect to the L^2 -scalar product on Ω is given by

$$N(W)^\perp = \{j \in H_{\text{div}=0}(\Omega)^3 : \exists q \in L^2(\Omega)^3 \text{ s. th. } \text{curl } j = \text{grad } q\} \quad (13)$$

with $H_{\text{div}=0} := \{v \in L^2(\Omega) : \text{div } v = 0\}$. Further, it has been shown that for a homogeneous conductivity distribution σ the solution of (6)-(9) is in $N(W)^\perp$ and, thus, in this case we obtain full reconstructability.

Our key goal here is to investigate appropriate conditions on the current density distributions j to reduce the ill-posedness of the inversion and to improve the reconstructions achieved in [12] by plain Tikhonov regularization. In particular, we study these three algorithms:

- (A) The plain Tikhonov regularization
- (B) The use of the condition (6) to supplement the equation (11).
- (C) The incorporation of the full boundary value problem (7) - (9) into equation (11).

We will show how the ill-posedness of the inversion is reduced via the conditions (B) and (C). In particular, a) we derive *qualitative* estimates of the singular values of the operators under consideration and b) we provide numerical results about the *quantitative* improvements which can be gained. These are compared with the improvements which can be achieved by changing central inversion parameters like the distance of the measurement points to the area Ω of the current density j .

We will introduce the discretized form of the Biot-Savart integral operator via a finite integration technique in Section 2, which serves as our toolbox for the subsequent sections. In Section 3 we discuss the methods (B) and (C). Section 4 serves to analyse and compare the stability for the algorithms under consideration by estimates for their singular values. Finally, in Section 5 we compare reconstruction results and we provide a numerical evaluation of the stability constants for real settings which is typically used for state-of-the-art devices of magnetic tomography.

2. Continuous and discrete realization of the Biot-Savart operator

The goal of this section is to summarize the finite integration technique applied to magnetic tomography. The convergence of the technique towards the solution of the continuous problem (1) - (5) has been analysed by Kühn et al [13]. Since the discretization is directly integrated into our inverse algorithms in the subsequent parts

we provide basic notation here and summarize the results. We will investigate the situation where

$$\Omega := \left\{ y \in \mathbb{R}^3, \frac{-a_1}{2} < y_1 < \frac{a_1}{2}, \frac{-a_2}{2} < y_2 < \frac{a_2}{2}, \frac{-a_3}{2} < y_3 < \frac{a_3}{2} \right\} \quad (14)$$

with some parameters $a_1, a_2, a_3 > 0$. We employ a discretization with levels n_1, n_2, n_3 in the direction of the x_1, x_2 or x_3 -axis, respectively. In Figure 3 (first row, left) we show an example for a $3 \times 4 \times 2$ discretization. This type of grid has a physical realization, for which the algorithms of magnetic tomography can be tested directly on real data. It corresponds to a resistor network of the same dimension, compare Figure 3 (first row, right) showing some physical realisation of a $5 \times 5 \times 4$ resistor network with a conductivity σ_1 in x-y-direction and $\sigma_2 \ll \sigma_1$ in z-direction which models the conditions in a fuel cell, where the conductivity through the membrane (z-direction) is lower than in the bipolar plates (x-y-plane). The numbering of knots and wires is shown in Figure 3 (first row, left and middle). The inflow and outflow knot of the current are located centered on the bottom, in the example in figure 3 at the knot 2 and 14 respectively.

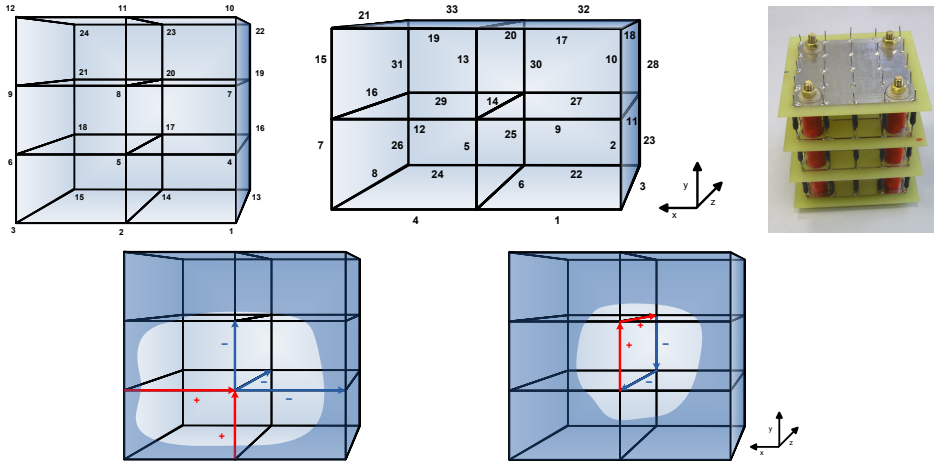


Figure 3. This is the discretization grid as it models the fuel cell in the software and its physical realization as a resistor network. First row: The images on the left hand side show the numbering of knots and wires, the image on the right hand side shows the resistor network. Second row: The image on the left hand side shows Kirchhoff's knot rule with the inflowing and outflowing currents for one knot. The image on the right hand side illustrates one mesh.

As known in standard circuit theory, a current flow in a resistor network can be calculated via *mesh* and *knot rules*, also known as *Kirchhoff's circuit laws*. Here, we used the adjacency matrix $\mathbf{T} = (T_{kl}), k = 1, \dots, K, l = 1, \dots, N$, where T_{kl} is 1 if wire l starts at knot k , -1 if wire l ends in knot k and 0 otherwise and the hand side $\mathbf{b} = (b_1, \dots, b_K)^T$ defined by

$$b_k = \begin{cases} I, & \text{if } k \text{ is the injection knot of the current} \\ -I, & \text{if } k \text{ is the outflow knot of the current} \\ 0, & \text{otherwise} \end{cases} \quad (15)$$

with the total current I . For the discrete model we assume that the resistance of wire l is given by R_l . The current J_l flowing through wire l , the resistance R_l of wire l and the voltage U_l between the two endpoints of wire l are connected via *Ohm's law*

$$U_l = R_l \cdot J_l. \quad (16)$$

The knot rules are then given by

$$\sum_{l=1}^N T_{kl} J_l = b_k, \quad k = 1, \dots, K. \quad (17)$$

The construction of the mesh rules has been realized as follows. For every knot k we take an outgoing wire in positive direction of an arbitrary axis that ends at knot \tilde{k} . Starting from \tilde{k} we take a wire in positive direction of an axis that is different to the one chosen before. Then the mesh is closed by choosing exactly two additional wires. By iterating this procedure over all knots we get the linear system

$$\sum_{l=1}^N S_{ml} (R_l J_l) = 0, \quad m = 1, \dots, M, \quad (18)$$

where S_{ml} is 1 if wire l is part of mesh m and the wire is passed through in positive direction and -1 if it is passed through in negative direction respectively. Otherwise S_{ml} is 0.

This procedure results in $3n_1n_2n_3 - n_1n_2 - n_1n_3 - n_2n_3 + 1$ equations for the $3n_1n_2n_3 - n_1n_2 - n_1n_3 - n_2n_3$ currents, with one redundant equation due to the solenoidality of the electric potential. Here, we drop the last equation to obtain a uniquely solvable system.

Having calculated the currents we are able to calculate the magnetic field at a point $x \in \mathbb{R}^3$ via the discrete Biot-Savart operator for this wire grid. This reduces to calculate

$$(\mathbf{WJ})(x) = -\frac{1}{4\pi} \sum_{\text{wires } l} \int_l \frac{\tilde{J}_l \times (x - p)}{|x - p|^3} ds(p), \quad (19)$$

with $\tilde{J}_l := (J_l, 0, 0)^T$, if wire l is parallel to the x-axis, $\tilde{J}_l := (0, J_l, 0)^T$, if wire l is parallel to the y-axis or $\tilde{J}_l := (0, 0, J_l)^T$, if wire l is parallel to the z-axis. Here, we have used an exact integration of the magnetic field for a straight wire as explicitly given by equation (4.9) in [5].

The convergence theorem for the *finite integration technique* towards the solution of the continuous problem (1) - (5) has been shown in [13], where the discretized problem is extended into the three-dimensional space via interpolation.

THEOREM 2.1 *Let σ be a coercitive matrix. Then the equation system arising from mesh and knot rules has a unique solution for each discretization (n_1, n_2, n_3) . For $n_j \rightarrow \infty, j = 1, 2, 3$ it converges towards the true solution of the boundary problem.*

3. Algorithms for magnetic tomography

The Biot-Savart operator W is a linear and bounded operator from $(L^2(\Omega))^3$ to $(L^2(\partial G))^3$. Since it has an analytic kernel it is well-known from standard functional analysis that it is a compact operator ([10], Thm. 2.21) with exponentially decaying singular values. It can not be continuously invertible ([10], Thm. 2.20). This leads to highly unstable reconstructions where small perturbations in the right hand side of (11) cause strong perturbations in the solution and is one of the main limitations of magnetic tomography.

Discretizing the Biot-Savart operator as described in the previous section we get the $3n \times N$ matrix \mathbf{W} , where n is the number of measurement points on the measurement surface ∂G and N is the number of wires in the cube. We usually assume $3n \gg N$, i.e. we work with overdetermined systems. Then, the discretized form of (11) is given by

$$\mathbf{W}\mathbf{J} = \mathbf{H}_{\text{meas}}. \quad (20)$$

It has been shown in [5] that \mathbf{W} is injective. However, this finite dimensional system is strongly ill-conditioned where the condition number increases exponentially when the approximation level is increased. The basic principle of *regularization methods* for injective operators is to approximate the unbounded operator W^{-1} by a bounded operator R_α with *regularization parameter* $\alpha > 0$ which shows pointwise convergence $R_\alpha H \rightarrow j := W^{-1}f, \alpha \rightarrow 0$, for $H = Wj$. If W is not injective, we cannot expect $R_\alpha H \rightarrow j$, but we usually we have $R_\alpha H \rightarrow Pj, \alpha \rightarrow 0$, with some projection operator P . For continuous Tikhonov regularization the projection P is the orthogonal projection onto $N(W)^\perp$. For the discrete case, classical Tikhonov regularization [17] employs

$$\mathbf{R}_\alpha := (\alpha\mathbf{I} + \mathbf{W}^*\mathbf{W})^{-1}\mathbf{W}^* \quad (21)$$

with regularization parameter $\alpha > 0$, where \mathbf{W}^* denotes the complex conjugate transpose matrix of \mathbf{W} . For the choice of the regularization parameter we refer to standard results in [3]. Plain Tikhonov regularization has been applied to magnetic tomography problem in [12] which proves in principle the feasibility of current reconstructions for the inverse problem (11), but also demonstrates its severe ill-posedness. We denote the classical algorithm (21) by \mathbf{A} . In the following subsections we combine projection algorithms where further knowledge is incorporated into the inversion procedure with Tikhonov type regularization schemes.

3.1. Divergence free Tikhonov regularization

We recall that the current distribution j is *divergence free* and it is natural to incorporate condition (6) into the inversion. We expect this condition to decrease the solution space to provide a more accurate solution and will provide qualitative estimates and quantitative results in the next sections.

For the discrete realization of the inversion we use the condition introduced in equation (17) for choosing the finite subset X_n of the solution space $(L^2(\Omega))^3$. This

condition corresponds to *Kirchhoff's knot rule*, so we set up the matrix \mathbf{T} as described in section 2. Since the discrete solution \mathbf{J} solves

$$\mathbf{T}\mathbf{J} = \mathbf{b}, \quad (22)$$

with a *particular solution* j_0 the *general solution* of this equation is given by

$$j_{gen} = j_0 + \mathbf{N}z, \quad (23)$$

with a basis \mathbf{N} of the nullspace of \mathbf{T} and arbitrary z . Inserting this representation into equation (20) we derive

$$(\mathbf{W}\mathbf{N})z = \mathbf{H}_{meas} - \mathbf{W}j_0 \quad (24)$$

which can be solved via Tikhonov regularization by setting

$$\mathbf{R}_\alpha := (\alpha\mathbf{I} + (\mathbf{W}\mathbf{N})^*(\mathbf{W}\mathbf{N}))^{-1}(\mathbf{W}\mathbf{N})^*, \quad \alpha > 0. \quad (25)$$

Now a solution \mathbf{J} of (20) can be obtained by setting

$$\mathbf{J} := j_0 + \mathbf{N}\mathbf{R}_\alpha(\mathbf{H}_{meas} - \mathbf{W}j_0). \quad (26)$$

A concise formulation of this algorithm is given by the following pseudo code.

Algorithm B. Divergence free Tikhonov regularization

function DIVERGENCEFREETIKHONOV($\alpha, \mathbf{b}, \mathbf{H}_{meas}$)

 calculate \mathbf{W} via finite integration

 calculate \mathbf{T} from (17)

 calculate particular solution j_0 of $\mathbf{T}\mathbf{J} = \mathbf{b}$

 calculate orthonormal basis \mathbf{N} of $N(\mathbf{T})$

$\mathbf{R}_\alpha \leftarrow (\alpha\mathbf{I} + (\mathbf{W}\mathbf{N})^*(\mathbf{W}\mathbf{N}))^{-1}(\mathbf{W}\mathbf{N})^*$

$\mathbf{J} \leftarrow j_0 + \mathbf{N}\mathbf{R}_\alpha(\mathbf{H}_{meas} - \mathbf{W}j_0)$

 return \mathbf{J}

end function

Numerical results for the algorithm are shown in section 5. We estimate the singular values of $\mathbf{W}\mathbf{N}$ in section 4.

3.2. A projection method with special basis functions

In this section we will take into account the information that our currents solve the boundary value problem (6) - (9). This leads to a projection method with a special basis $\{j^{(k)} : k = 1, \dots, N\}$. Here, we construct this basis such that its z -components approximately build a Haar basis, i.e. they are approximately a multiple of 1 in some section and close to zero in all others.

As background we remind the reader that for the fuel cell application the conductivity in $x - y$ layers are usually large and uniform due to metallic end plates and carbon layers between the different single fuel-cells. Thus, we use a uniform high conductivity σ_0 in all wires in $x - y$ direction. We have varying conductivity only in the

wires in z -direction, which we label from $k = 1$ to $k = N$. Now, we choose numbers σ_l , $l = 0, 1, 2$ with

$$\sigma_2 \ll \sigma_1 \ll \sigma_0. \quad (27)$$

Then, the idea is to use the ansatz

$$j = \sum_{k=1}^N \xi_k j_k, \quad (28)$$

where j_k is a current distribution with a conductivity which is set to σ_1 in wire k in z -direction and to σ_2 in all other wires in z -direction. We use the notation $X_N := \text{span}\{j_k : k = 1, \dots, N\}$. The current distributions $j_k, k = 1, \dots, N$ are solutions to the forward problem, i.e. they are calculated via *knot* and *mesh rules* as described in section 2. The magnetic field of an element $j \in X_N$ at a point $x \in \mathbb{R}^3$ can be calculated via

$$(\mathbf{W}j)(x) = \sum_{k=1}^N \xi_k (\mathbf{W}j_k)(x). \quad (29)$$

Defining $H_k := \mathbf{W}j_k$ by evaluating the Biot-Savart operator, we set up the matrix $\mathbf{H}_s := (H_1, \dots, H_N)$. Then, we solve the ill-posed linear system

$$\mathbf{H}_s \xi = \mathbf{H}_{\text{meas}} \quad (30)$$

for the coefficients $\xi := (\xi_1, \dots, \xi_N)^T$, where we employ Tikhonov regularization for regularization of this system. The solution \mathbf{J} of the original problem is obtained by calculating

$$\mathbf{J} := \sum_{k=1}^N \xi_k j_k. \quad (31)$$

In view of Section 4, Theorem 4.4, we note that in general the j_k are not an orthonormal basis of the discrete space X_N . However, we can orthonormalize j_k to obtain a basis $\{j_{k,o} : k = 1, \dots, N\}$ of X_N and define $\mathbf{H}_{s,o} := (\mathbf{W}j_{1,o}, \dots, \mathbf{W}j_{N,o})$. Then all estimates below apply. However, for simplicity we have usually directly applied the special basis method via \mathbf{H}_s with satisfying results. We conclude this section with the pseudo code presentation of the special basis projection method.

Algorithm C. Special basis projection

```

function SPECIALBASISPROJECTION( $\alpha, \mathbf{H}_{\text{meas}}$ )
  calculate  $\mathbf{W}$  via finite integration
  for  $k = 1, \dots, N$  do
    calculate current distribution  $j_k$  as described in (27)
     $H_k \leftarrow \mathbf{W}j_k$ 
  end for
   $\mathbf{H}_s := (H_1, \dots, H_N)$ 
   $\mathbf{R}_\alpha \leftarrow (\alpha \mathbf{I} + \mathbf{H}_s^* \mathbf{H}_s)^{-1} \mathbf{H}_s^*$ 
   $\xi \leftarrow \mathbf{R}_\alpha \mathbf{H}_{\text{meas}}$ 
   $\mathbf{J} \leftarrow \sum_{k=1}^N \xi_k j_k$ 
  return  $\mathbf{J}$ 
end function

```

Numerical results for the algorithm are shown in section 5 and we estimate the singular values of the orthonormalized version $\mathbf{H}_{s,o}$ of \mathbf{H}_s in section 4.

4. Algorithmic stability analysis in dependence on a priori knowledge

In this section we study the stability of the above algorithms via their singular values and derive estimates for the singular values of the methods.

Usually, for estimating the ill-posedness of inverse problems the size of the singular values is taken as central measure. For discrete inverse problems the condition number is the key quantity. Here, we are mostly interested in the singular values as becomes clear from the following reasons. Consider an equation

$$Ax = b \tag{32}$$

which we solve with some data error $e^{(\delta)}$, i.e. we calculate $x^{(\delta)}$ by

$$A(x^{(\delta)}) = b + e^{(\delta)}. \tag{33}$$

In general one estimates the error by

$$\|x - x^{(\delta)}\| \leq \|A^{-1}\| \cdot \|e^{(\delta)}\| \tag{34}$$

and calculates the relative error

$$\frac{\|x - x^{(\delta)}\|}{\|x\|} \leq \|A^{-1}\| \cdot \|A\| \cdot \frac{\|e^{(\delta)}\|}{\|b\|}. \tag{35}$$

Thus, the condition number provides an upper bound for the relative numerical error. Now, we consider two matrices A_1, A_2 with $A_1 x = b$ and $A_2 x = b$, where the singular values of A_2 are larger than the singular values of A_1 , thus the norm $\|A_2^{-1}\|$ is smaller than the norm $\|A_1^{-1}\|$. Still, the condition of A_2 might be larger than the condition of A_1 , which is partly the case for our setting of magnetic tomography. If we solve the

same problem with given data we need to consider the case where we keep $e^{(\delta)}$ fixed. Then, we solve the systems

$$A_1 x_1^{(\delta)} = b + e^{(\delta)}, \quad A_2 x_2^{(\delta)} = b + e^{(\delta)}, \quad (36)$$

Estimating the reconstruction error $\|x - x^{(\delta)}\|$ as in (34) we have

$$\|A_2^{-1}\| \cdot \|e^{(\delta)}\| \leq \|A_1^{-1}\| \cdot \|e^{(\delta)}\|, \quad (37)$$

i.e. we have a better estimate for the data error from the second system with A_2 than for the system with A_1 . Here, the true solution x is fixed. In this case from (37) we get a better estimate for the relative error via the second system

$$\frac{\|x - x_2^{(\delta)}\|}{\|x\|} \leq \frac{\|A_2^{-1}\| \cdot \|b\| \|e^{(\delta)}\|}{\|x\| \|b\|}, \quad (38)$$

compared to the estimate for the first system

$$\frac{\|x - x_1^{(\delta)}\|}{\|x\|} \leq \frac{\|A_1^{-1}\| \cdot \|b\| \|e^{(\delta)}\|}{\|x\| \|b\|}. \quad (39)$$

If the error is a multiple of the eigenvector with smallest singular value of A_1 , then the estimate (39) will be sharp and the improvement in the error is fully given by the improvement in the estimate (37) of the norm of the inverse via the singular values. The estimate (38) fully carries over to (24): one calculates

$$\begin{aligned} (WN)z &= H_{meas} - Wj_0 \Rightarrow (WN)(z - z^{(\delta)}) = e^{(\delta)} \\ &\Rightarrow x - x^{(\delta)} = N(z - z^{(\delta)}) = N(WN)^{-1}e^{(\delta)} \end{aligned} \quad (40)$$

Since N has orthonormal columns we obtain (38) also for a setting of the form (24).

For general estimates of the singular values we will use the Courant minimum maximum principle as a key tool. First, we order the eigenvalues of a self-adjoint matrix operator $A : \mathbb{C}^n \rightarrow \mathbb{C}^n$ according to their size and multiplicity $\lambda_1 \geq \lambda_2 \geq \dots \geq \lambda_n$. Then, the Courant minimum maximum principle states that

$$\lambda_{n+1-k} = \min_{\dim U=k} \max_{x \in U} \frac{(Ax, x)}{(x, x)}, \quad k = 1, \dots, n. \quad (41)$$

We use this to prove some useful properties. Roughly speaking, the aim of this section is to show that incorporating some a priori knowledge leads to larger singular values of the corresponding Tikhonov matrix. We set up a general framework in terms of subspaces and apply this to our setting of magnetic tomography.

DEFINITION 4.1 (A PRIORI KNOWLEDGE VIA SUBSPACE SETTING) *We denote $X = \mathbb{C}^n$ and $Y = \mathbb{C}^m$ and we consider an operator $W : X \rightarrow Y$. For a subspace $V \subset X = \mathbb{C}^n$ we define $W_V : V \rightarrow Y$ by $W_V = W|_V$ and W_V^* to be its adjoint operator $Y \rightarrow V$ determined by*

$$(Wx, y)_Y = (x, W_V^*y)_V, \quad x \in V, y \in Y. \quad (42)$$

It is well known that

$$N(W_V^*) = W(V)^\perp. \quad (43)$$

Clearly, the operator $A_V := W_V^* W_V$ is a self adjoint operator on V , since for $x, z \in V$ we have

$$(z, W_V^* W_V x)_V = (W_V z, W_V x)_Y = (W_V^* W_V z, x)_V. \quad (44)$$

First, we collect some properties of the adjoint operators arising from the subspaces $\tilde{V} \subset V \subset X$.

LEMMA 4.2 *Let $\tilde{V} \subset V \subset X$ be subspaces and consider the adjoint operators W_V^* of $W_V : V \rightarrow Y$ and $W_{\tilde{V}}^*$ of $W_{\tilde{V}} : \tilde{V} \rightarrow Y$ arising from the restriction of W to V or \tilde{V} , respectively. Further, let $P : V \rightarrow \tilde{V}$ denote the orthogonal projection operator from V onto $\tilde{V} \subset V$. Then we obtain*

$$W_{\tilde{V}}^* = P W_V^*. \quad (45)$$

Proof. We denote $Q := I - P$ and decompose $x = Qx + Px$ for $x \in V$. For $x \in \tilde{V}, y \in Y$ we obtain $Qx = 0$ and in this case we calculate

$$\begin{aligned} (x, P W_V^* y) &\stackrel{P=I-Q}{=} (x, W_V^* y - Q W_V^* y) \stackrel{Qx=0}{=} (Px, W_V^* y - Q W_V^* y) \\ &\stackrel{P(V) \perp Q(V)}{=} (x, W_V^* y) = (W_V x, y) \stackrel{x \in \tilde{V} \subset V}{=} (W_{\tilde{V}} x, y) = (x, W_{\tilde{V}}^* y). \end{aligned} \quad (46)$$

This yields $(x, (P W_V^* - W_{\tilde{V}}^*) y) = 0$ for all $x \in \tilde{V}$, from which (45) follows. \square

We now prove a monotonicity property for singular values which directly applies to the setting of magnetic tomography.

THEOREM 4.3 *Let $V, \tilde{V} \subset \mathbb{C}^n$ be subspaces of \mathbb{C}^n with $\tilde{V} \subset V$ and denote the singular values of W_V or $W_{\tilde{V}}$, respectively, by μ_j or $\tilde{\mu}_j$, $j = 1, 2, 3, \dots$. We denote the dimensions of V, \tilde{V} by n, \tilde{n} and note that $\tilde{n} \leq n$ by $\tilde{V} \subset V$. Then we obtain the estimates*

$$\mu_{n+1-j} \leq \tilde{\mu}_{\tilde{n}+1-j}, \quad j = 1, 2, 3, \dots, \tilde{n}. \quad (47)$$

Moreover, in this estimate we will obtain equality for $k \in \mathbb{N}$ if and only if the eigenspace E_k of $W_V^ W_V$ with eigenvalue λ_{n+1-k} is a subset of \tilde{V} .*

Proof. We employ the Courant minimum maximum principle applied to the eigenvalues λ_k of $W_V^* W_V$ and the eigenvalues $\tilde{\lambda}_k$ of $W_{\tilde{V}}^* W_{\tilde{V}}$ to derive

$$\begin{aligned} \lambda_{n+1-k} &= \min_{U \subset V, \dim U = k} \left(\max_{x \in U} \frac{(W_V^* W_V x, x)}{(x, x)} \right) \\ &= \min_{U \subset V, \dim U = k} \left(\max_{x \in U} \frac{(W_V x, W_V x)}{(x, x)} \right) \\ &\leq \min_{U \subset \tilde{V}, \dim U = k} \left(\max_{x \in U} \frac{(W_V x, W_V x)}{(x, x)} \right) \\ &= \min_{U \subset \tilde{V}, \dim U = k} \left(\max_{x \in U} \frac{(W_{\tilde{V}} x, W_{\tilde{V}} x)}{(x, x)} \right) \\ &= \min_{U \subset \tilde{V}, \dim U = k} \left(\max_{x \in U} \frac{(W_{\tilde{V}}^* W_{\tilde{V}} x, x)}{(x, x)} \right) \\ &= \tilde{\lambda}_{\tilde{n}+1-k} \end{aligned} \quad (48)$$

for $k = 1, 2, \dots, \tilde{n}$. In this estimate we will obtain equality for $k \in \mathbb{N}$ if and only if all subspaces U with a dimension $\dim(U) = k$ of the eigenspace E_k corresponding to the eigenvalue λ_{n+1-k} (which are spaces U where the Courant minimax principle attains its minimum) are subsets of \tilde{V} . This is equivalent to the eigenspace E_k being a subset of \tilde{V} . \square

We apply the result to our algorithms for magnetic tomography as follows.

THEOREM 4.4 *Consider the three solution methods (A), (B) and (C) from Section 1:*

- (A) *the plain Biot-Savart equation given by (20),*
- (B) *the divergence free Biot-Savart equation as in (24) and*
- (C) *the special basis Biot-Savart equation (30).*

Here, for (30) we assume that the basis currents j_1, \dots, j_N build an orthonormal set in the space of all currents. Then for the singular values $\mu_k^{(A)}$, $\mu_k^{(B)}$ and $\mu_k^{(C)}$ of the matrices $\mathbf{W}^{(A)} := \mathbf{W}$, $\mathbf{W}^{(B)} := \mathbf{WN}$ and $\mathbf{W}^{(C)} := \mathbf{H}_{s,o}$ we obtain the estimates

$$\mu_{n_A+1-k}^{(A)} \leq \mu_{n_B+1-k}^{(B)} \leq \mu_{n_C+1-k}^{(C)} \quad (49)$$

for $k = 1, 2, \dots, n_C$.

Proof. The generic case is provided by a matrix \mathbf{W} and a matrix \mathbf{N} with orthonormal columns. In this case we can interpret the mapping $z \mapsto \mathbf{N}z$ as a restriction of the mapping \mathbf{W} to the image space $V := \{v_1, \dots, v_m\}$ where v_j are the columns of \mathbf{N} . Let $U \subset \mathbb{C}^m$ be a subset. Then

$$\min_{U \subset \mathbb{C}^m, \dim U = k} \left(\max_{z \in U} (\mathbf{WN}z, \mathbf{WN}z) \right) = \min_{\tilde{U} \subset V, \dim \tilde{U} = k} \left(\max_{x \in \tilde{U}} (\mathbf{WN}x, \mathbf{WN}x) \right) \quad (50)$$

with $V := N(\mathbb{C}^m)$, because \mathbf{N} maps the set of subspaces of \mathbb{C}^m bijectively onto the set of subspaces of V . From this follows that \mathbf{WN} and $\mathbf{W}|_V$ have the same singular values.

The mapping $z \mapsto \mathbf{N}z$ is norm preserving. Now, an application of Theorem 4.3 proves an estimate of the form (49).

For the comparison of (B) and (C) we remark that the matrix arising from $\mathbf{W}j_k$ can be written as \mathbf{WJ} with the orthonormal matrix $\mathbf{J} = (j_1, \dots, j_N)$. We remark that since the j_k are calculated from equations (17) and (18) are divergence free. The estimate is then obtained as above from Theorem 4.3. \square

We have shown that the use of a priori knowledge via knot equations and special basis functions which incorporate the background knowledge leads to better estimates for inversion than the general Biot-Savart equation. Moreover, the estimate of the singular values provides a strong spectral analysis of the situation, which can be used in more detail. Here, we next will provide a numerical study of the situation which confirms the above estimates and also demonstrates the actual size of the constants for some important sample settings frequently used for the practical application of magnetic tomography.

5. Evaluation of stability constants for a realistic setup

We use a $7 \times 7 \times 2$ -grid to simulate a single-cell device as presented in figure 4. 296 measurement points are placed equidistantly in distance of 60 mm around the wire grid.

In the following we will present a numerical spectral analysis done for this important sample setting. Figure 5 shows the singular values of the matrices \mathbf{W} , \mathbf{WN} and \mathbf{H}_s that were presented in section 3 for this setting. In this example the magnitude of the smallest singular values differ by a factor between 10 and 100 as well between algorithms (A) and (B) as between algorithms (B) and (C).

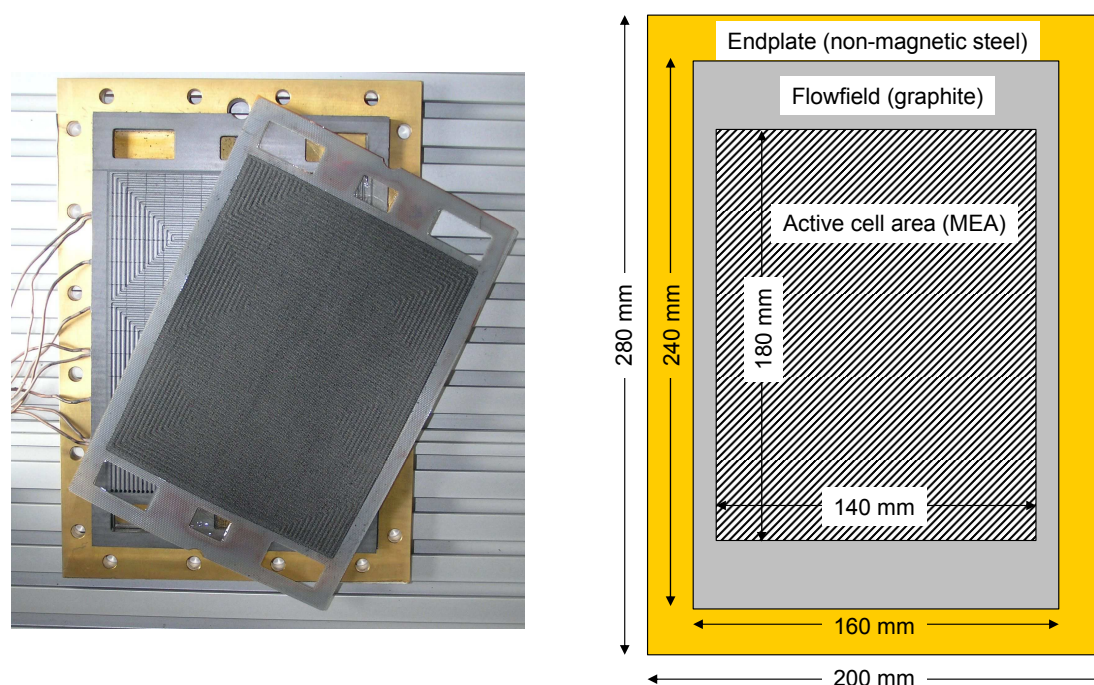


Figure 4. Real cell components (endplate, flowfield and membrane electrode assembly (MEA)), dimension of the cell components.

Figure 6 shows a comparison of the reciprocal of the singular values of each matrix and the singular values of the corresponding Tikhonov matrix.

We expect, that the ill-posedness of the problem decreases, when the observation distance is reduced. We present a short overview in which manner this happens by showing reconstruction errors for different observation distances and a comparison of the singular values, where the distance between the measurement surface and the measured object is reduced to 30 mm. The size of the singular values differs by a factor of 100 uniformly over all three methods by halvening the distance between the measurement surface and the measured object. The behavior of the reciprocal of the singular values compared to the singular values of the Tikhonov matrix is illustrated in figure 7. Table 1 shows reconstruction errors for the sample setting mentioned above for the measurement

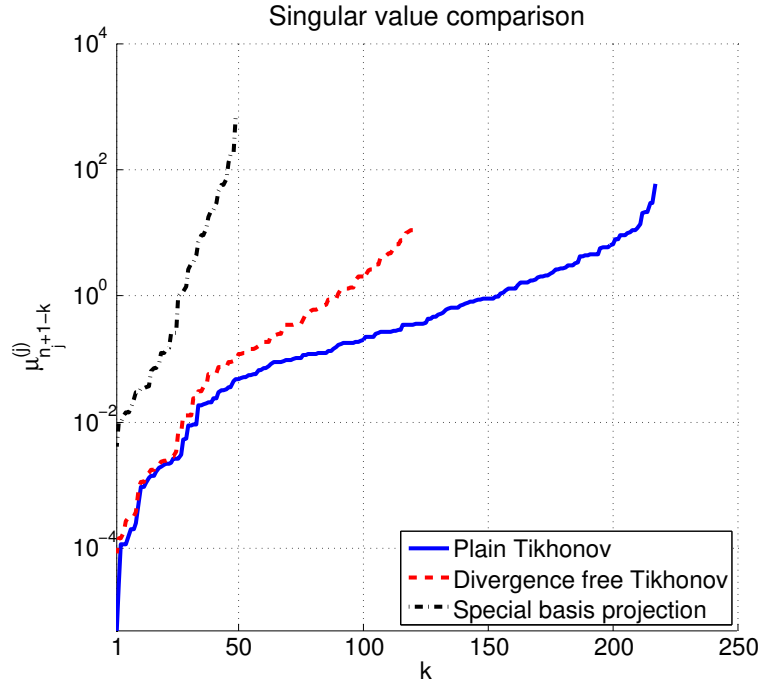


Figure 5. Comparison of the singular values of \mathbf{W} , \mathbf{WN} and \mathbf{H}_s . The measurement points are placed in a distance of 60 mm around the resistor network. We illustrate Equation (49) with $j = A, B, C$ corresponding to the presented methods.

points placed in a distance of 60 mm, 45 mm, 30 mm and 15 mm of the measured object. The calculated magnetic field is disturbed by a uniformly distributed *relative error* of 5 % in the data in the discrete L^2 -norm $\|\cdot\|_2$.

Table 1. Average reconstruction errors for different distances of the measurement points with constant relative right hand side error of 5 %. For each reconstruction we used the best possible choice of the regularization parameter α , which has been calculated using the full knowledge of the true solution to the problem.

| Method | 60 mm | 45 mm | 30 mm | 15 mm |
|---|---------|---------|---------|--------|
| Plain Tikhonov Regularization | 17.07 % | 13.47 % | 12.23 % | 7.07 % |
| Divergence free Tikhonov Regularization | 15.76 % | 12.81 % | 12.04 % | 6.36 % |
| Special basis reconstruction method | 9.75 % | 7.81 % | 6.65 % | 5.53 % |

Next we present some reconstructions comparing the three methods (A) - (C). For generating sample currents we lowered the conductivity in z-direction at two wires in the interior. The resulting current distribution and the magnetic field are calculated according to section 2. Figure 8 (top left) visualizes this current distribution. The simulated magnetic field is disturbed by a uniformly distributed random error vector with maximum 7 % of the maximal magnetic field strength. For this error size the average current density is 125 mA/cm^2 which corresponds to the DMFC (*direct methanol*

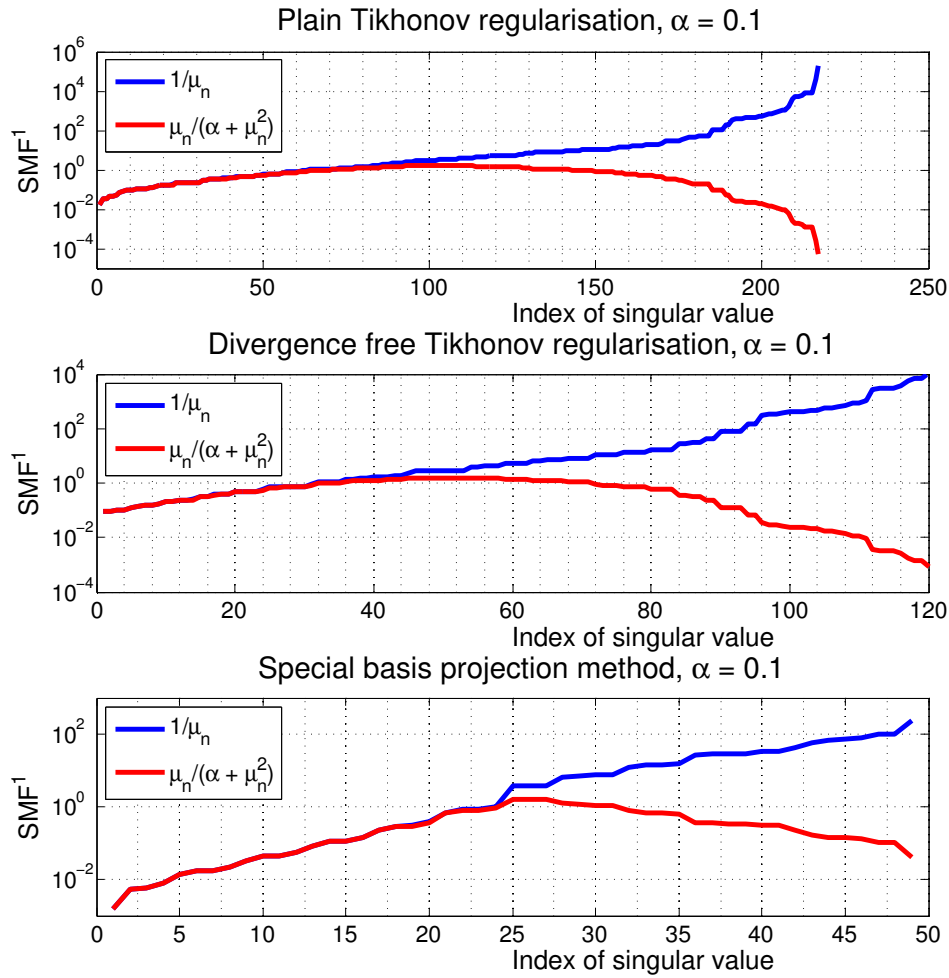


Figure 6. Reciprocal of the singular values of the original matrix and the singular values of the Tikhonov operator with distance of 60 mm between measurement points and resistor network

¹ SMF = Spectral multiplication factor

fuel cell) application, but the range in figure 8 is cut at $40\text{mA}/\text{cm}^2$ to make artefacts visible.

One can see clearly the improvements resulting from incorporating a priori knowledge as described and analyzed in sections 3 and 5. The plain Tikhonov regularization (method (A)) identifies the spots with lowered current density correctly, but generates strong artefact in the neighborhood of the real spots. The divergence free Tikhonov regularization (method (B)) also identifies regions with lowered current density, but the two distinctly separated wires appear as one area with lower current density. There are also some artefacts surrounding the identified spots. As expected from the results of section 5 the special basis projection method (method (C)) provides the best reconstruction results. One can see two clearly separated spots and a reduction of the artefacts.

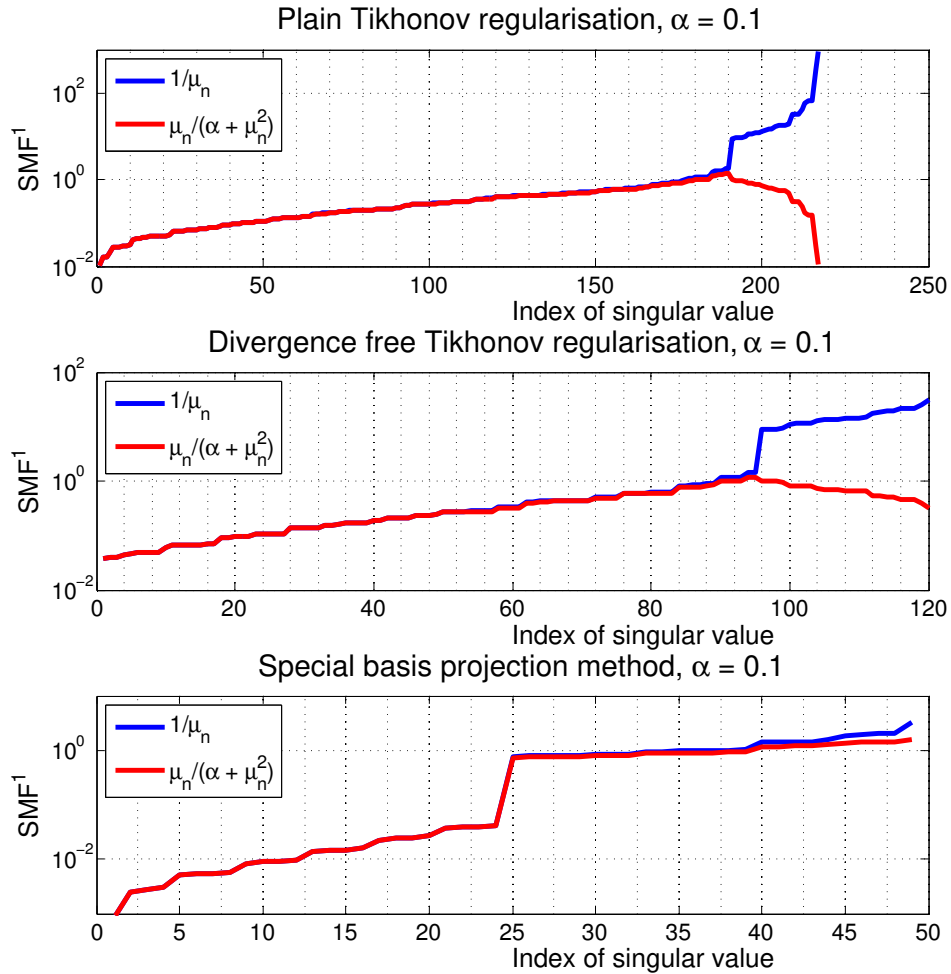


Figure 7. Reciprocal of the singular values of the original matrix and the singular values of the Tikhonov operator with distance of 30 mm between measurement points and resistor network.

¹ SMF = Spectral multiplication factor

6. Summary and Outlook

We have shown that incorporating some a priori knowledge about the current density leads to significantly better reconstruction results. In detail, we presented and compared three different reconstruction schemes and derived estimates for the singular values of the corresponding operators. The *special basis projection technique*, where most a priori knowledge is incorporated, shows the best reconstruction results. We provide explicit estimates and values for a practically relevant setting.

Our estimates and simulations will stimulate future research and development:

- (i) Reducing the distance of the measurement surface to the measured object reduces the ill-posedness of the underlying problem, so in the practical application of magnetic tomography for fuel cells new sensors (or sensor heads) have to be developed to allow measurements close to the fuel cell.

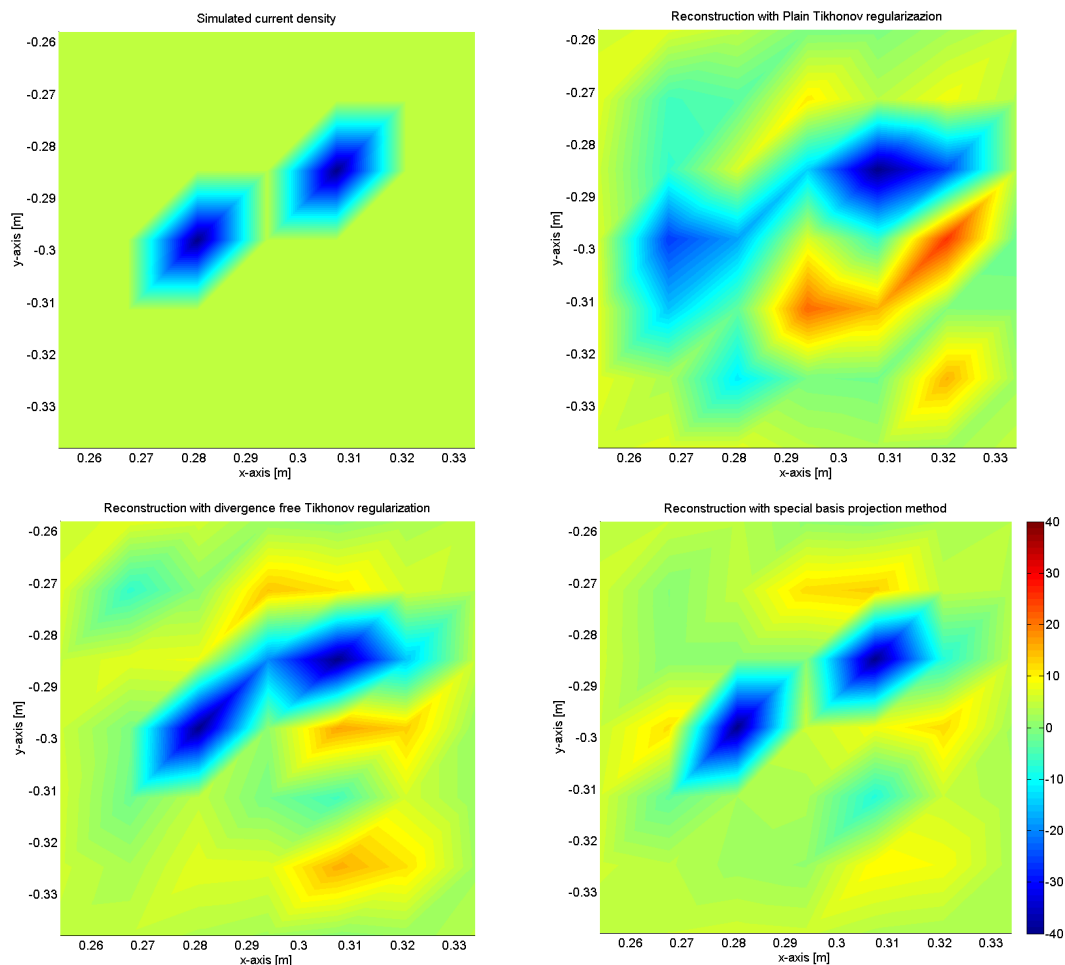


Figure 8. From top left to bottom right: Initial current distribution, Reconstructions via plain Tikhonov regularization (method A), divergence free Tikhonov regularization (method (B)) and special basis projection method (method (C)). For each reconstruction we used the best possible choice of the regularization parameter α , which has been calculated using the full knowledge of the true solution to the problem.

- (ii) We have presented a qualitative estimate for the singular values, what tools can be developed to derive quantitative estimates?
- (iii) It remains as an open question how errors in the a priori knowledge influence the reconstructions.
- (iv) Which other techniques exist to incorporate a priori knowledge and how do these prospective methods compare to methods (A), (B) and (C).

Acknowledgements

This work has in part been supported by the Fuel Cell Initiative Lower-Saxony, Germany, under the grant number 80013461.

References

- [1] Colton D and Kress R 1998 *Inverse Acoustic and Electromagnetic Scattering Theory (Applied Mathematical Sciences vol 93)*, 2nd edn (Berlin: Springer)
- [2] Del Gratta C, Pizzella V, Tecchio F and Romani G L 2001 Magnetoencephalography - a noninvasive brain imaging method with 1 ms time resolution *Rep. Prog. Phys.* **64** 1759–1814
- [3] Engl H W, Hanke M and Neubauer A 1996 *Regularization of inverse problems* (Dordrecht: Kluwer)
- [4] Hämmäläinen M, Hari R, Ilmoniemi R J, Knuutila J and Lounasmaa O V 1993 Magnetoencephalography - theory, instrumentation, and applications to noninvasive studies of the working human brain *Rev. Mod. Phys.* **65** 413–97
- [5] Hauer K-H, Kühn L and Potthast, R 2005 On uniqueness and non-uniqueness for current reconstruction from magnetic fields *Inverse Problems* **20** 1–13
- [6] Hauer K-H, Potthast R, Stolten D and Wüster T 2005 Magnetotomography - a new method for analysing fuel cell performance and quality *Journal of Power Sources* **143** 67–74
- [7] Potthast R and Wannert M Uniqueness of Current Reconstructions for Magnetic Tomography in Multi-Layer Devices, submitted for publication
- [8] Kaipio J, Somersalo E 2005 *Statistical and Computational Inverse Problems Applied Mathematical Sciences vol 160* (Berlin: Springer)
- [9] Kirsch A 1996 *An introduction to the mathematical theory of inverse problems (Applied Mathematical Science vol. 120)*, Berlin: Springer
- [10] Kress R 1999 *Linear Integral Equations (Applied Mathematical Sciences vol 82)*, 2nd ed (Berlin: Springer)
- [11] Kühn L 2005 Magnetic tomography - on the nullspace of the Biot-Savart operator and point sources for field and domain reconstruction *PhD Thesis* University of Göttingen
- [12] Kühn L, Kreß R and Potthast R 2002 The reconstruction of a current distribution from its magnetic fields *Inverse Problems* **18** 1127–46
- [13] Kühn L and Potthast R 2003 On the convergence of the finite integration technique for the anisotropic boundary value problem of magnetic tomography *Math. Meth. Appl. Sciences* **26** 739–57.
- [14] Lustfeld H, Reissel M, Schmidt U and Steffen B Reconstruction of electric currents in a fuel cell by magnetic field measurements *J. Fuel Cell Sci. Technol.*, accepted for publication
- [15] Potthast R 2006 A survey on sampling and probe methods for inverse problems. Topical Review *Inverse Problems* **22** R1-47
- [16] Sarvas J 1987 Basic mathematical and electromagnetic concepts of the biomagnetic inverse problem *Phys. Med. Biol.* **32** 11–22
- [17] Tikhonov A N 1962 On the solution of incorrectly formulated problems and the regularization method *Soviet Math. Doklady* **4** 1035–38, english translation